Elucidating conduction regimes and Joule heating performance in carbon-cement composites modified with acetylene black

Fairouz Touati, Daniel Ferry, Olivier Grauby, Philippe Papet, Gwenn Le Saout, Bertrand Wattrisse, Katerina Ioannidou

Construction and Building Materials 506 (2026) 144822

Contents lists available at ScienceDirect

Construction and Building Materials

journal homepage: www.elsevier.com/locate/conbuildmat

Elucidating conduction regimes and Joule heating performance in carbon-cement composites modified with acetylene black

Fairouz Touati [a], Daniel Ferry [b], Olivier Grauby [b], Philippe Papet [c], Gwenn Le Saout [d], Bertrand Wattrisse [a], Katerina Ioannidou [a,*]

[a] LMGC, Univ. Montpellier, CNRS, 860 Rue de St-Priest, Montpellier, 34090, France
[b] Aix Marseille Univ, CNRS, CINAM, Marseille, France
[c] ICGM, University Montpellier, CNRS, ENSCM, 1919 route de Mende, Montpellier, 34293, France
[d] LMGC, IMT Mines Ales, Université Montpellier, CNRS, Ales, 30100, France

ARTICLE INFO

Keywords:
Cementitious composites
Acetylene black
Percolation theory
Electrical properties
Joule heating
Self-heating materials
Microstructure

ABSTRACT

Developing multifunctional, self-heating cementitious composites is a key strategy for creating sustainable infrastructure and mitigating the environmental damage caused by de-icing salts. We fabricated composites using Portland cement and high-structure acetylene black as a conductive nanofiller (0–7 wt%) and analyzed their performance through systematic thermo-electric measurements, scanning electron microscopy, and a two-regime percolation model. The results demonstrate a percolation threshold (p_c) at approximately 2.5 wt% AB, above which the electrical conductivity increases by eight orders of magnitude to nearly 1 S/m. Our analysis reveals a distinct microstructural transition from a rapid-onset percolation regime (low exponent t_1) to a complex network consolidation regime (higher exponent t_2). In Joule heating tests, the composites achieved a maximum temperature increase (ΔT_{max}) of approximately 50 °C. Crucially, the maximum temperature gain plateaus at filler concentrations above 5 wt%, revealing a complex, non-linear relationship between electrical conductivity and steady-state thermal output. A quantitative comparison with literature benchmarks reveals that the AB-based composite possesses a remarkably high intrinsic heating efficiency, orders of magnitude greater than other carbon-based systems. This work provides a quantitative framework that directly links filler content, microstructure, and multifunctional performance in cement-nanocarbon composites, offering a basis for optimizing these materials to achieve both rapid heating and energy efficiency for practical applications.

1. Introduction

Cement-based materials are the cornerstone of global infrastructure, a status that brings with it significant environmental and maintenance responsibilities [1]. In regions with cold climates, a major challenge is reliance on deicing salts, which have well-documented corrosive effects on infrastructure and detrimental impacts on the surrounding environment [2–6]. A promising solution to this long-standing problem lies in the transformation of concrete from a passive structural element into an active functional material capable of self-heating through the Joule effect [7].

The key to unlocking such functionalities is the incorporation of nano-scale conductive fillers to create electrically conductive cementitious composites [8,9]. This approach has led to the field of smart and multifunctional concrete, with significant research dedicated to developing self-heating systems for deicing and pavement heating [10–14]. However, this requires fundamentally altering the nature of the cement paste itself. The hydrated cement matrix is a complex porous medium whose primary binding phase, calcium-silicate-hydrate (C-S-H), forms a disordered colloidal network, making it an excellent electrical insulator [15–17].

The effectiveness of creating a conductive composite is therefore not uniform; it depends critically on the intrinsic properties and dispersion quality of the chosen filler [18]. Electrical properties are governed by the percolation theory, where a critical concentration of filler must be reached to form a continuous network [19,20]. The efficiency with which this network forms and transports charge is deeply influenced by the morphology of the filler: its particle size, surface chemistry, and three-dimensional structure [21]. Furthermore, even once a network is established, the conduction mechanism itself can evolve. It can transition from a state limited by high interfacial resistance, where tunneling or hopping dominates, to a state governed by direct Ohmic-like transport, which can affect the universality of the scaling exponents [22–

* Corresponding author.
E-mail address: aikaterini.ioannidou@umontpellier.fr (K. Ioannidou).

https://doi.org/10.1016/j.conbuildmat.2025.144822
Received 27 August 2025; Received in revised form 23 November 2025; Accepted 6 December 2025
Available online 16 December 2025

24]. A comprehensive understanding of this transition is essential for designing materials with optimized thermo-electrical performance.

The state-of-the-art in this field has demonstrated the viability of various carbonaceous fillers, each with distinct trade-offs. Although carbon nanotubes (CNTs) possess exceptional intrinsic properties, their practical use is often hindered by prohibitive costs and significant challenges in achieving uniform dispersion within the cement matrix [25, 26]. Similarly, nanoengineering with graphene has led to composites with exceptional improvements in mechanical strength and water impermeability, demonstrating the broad potential of carbon nanomaterials [27]. In contrast, high-structure carbon blacks (CB), and particularly acetylene black (AB), offer a compelling alternative. AB is characterized by its high purity (> 99%), high crystallinity, and extremely high-structure aggregation of nanoparticles, allowing it to form conductive networks efficiently [21]. Notably, AB-based conductive cement has recently been patented as an electron-conducting composite material [28], underscoring its technological relevance for scalable self-heating cementitious systems. However, a common thread in many of these studies is a focus on the final thermal output, while the underlying electrical behavior is typically characterized using a simplified single-regime percolation model [19].

Despite extensive research into conductive cementitious composites, a significant gap remains in quantitatively linking the filler's microstructural arrangement to the macroscopic thermo-electrical behavior. Although fillers such as CNTs and graphene have been explored, they often face challenges with cost and dispersion. Acetylene black, with its unique high-structure morphology, offers a promising alternative, yet its performance is often analyzed using a standard single-regime percolation model, which fails to capture the complex conduction mechanisms at play. This study aims to fill this gap by: systematically characterizing the thermo-electrical properties of AB-cement composites; employing a two-regime percolation model that accurately captures the physical evolution of the conductive network from an exceptionally efficient, rapid-onset state (low exponent t_1) to a complex network densification regime (higher exponent t_2); and directly correlating these electrical regimes to the material's microstructure and its resulting Joule heating performance. In doing so, this work provides a deeper physical insight and a more accurate predictive framework to optimize these multifunctional materials.

2. Methods

The overall workflow of this study, from material preparation to final thermo-electrical analysis, is summarized in the flowchart in Fig. 1.

Photographs of the key experimental setups for thermal and electrical characterization are provided in the Supplementary Information (Figs. S1 and S2).

2.1. Sample preparation

2.1.1. Materials

The composite and reference samples were prepared using Portland cement (CEM I provided by Titan Cement). Two types of carbonaceous fillers were investigated. The primary filler was Acetylene Black (AB) powder (Soltex), characterized by its high purity (> 99% carbon), density of $1.7\,g\,cm^{-3}$ to $1.9\,g\,cm^{-3}$ and BET surface area of $100\,m^2\,g^{-1}$ to $120\,m^2\,g^{-1}$. For comparative analysis, a furnace black, PBX® 135 (Cabot Corporation), was also used. PBX 135 exhibits a BET surface area of $120\,m^2\,g^{-1}$ to $180\,m^2\,g^{-1}$ and an Oil Adsorption Number (OAN) of 150 mL/100g to 180 mL/100g, indicative of its structure.

The morphology of the as-received AB powder was characterized by scanning electron microscopy, as shown in Fig. 2. The micrograph, taken at 30,000 magnification, reveals that the filler is composed of spherical primary nanoparticles, approximately 30–50 nm in diameter, which are fused together into branched, chain-like aggregates. This aciniform, high-structure morphology is characteristic of AB. For the large-scale tile experiment, a polynaphthalene sulfonate (PNS) based superplasticizer was used to improve workability.

Table 1
Compositions of AB cement-carbon pastes studied for thermo-electrical properties. Three water/cement ratios were formulated with different carbon content ranging from 0 to 7% wt per total mass.

w/c	Cement (g)	Water (g)	AB (g)
w/c = 0.42 Series			
0.42	70.42	29.58	0
0.42	69.72	29.28	1
0.42	69.01	28.99	2
0.42	68.31	28.69	3
0.42	67.61	28.39	4
w/c = 0.6 Series			
0.6	62.50	37.50	0
0.6	61.81	37.09	1.10
0.6	61.53	36.92	1.55
0.6	61.13	36.68	2.20
0.6	60.46	36.28	3.26
0.6	59.81	35.88	4.31
0.6	59.03	35.42	5.55
0.6	58.38	35.03	6.60
w/c = 0.8 Series			
0.8	55.56	44.44	0
0.8	54.79	43.83	1.38
0.8	54.47	43.58	1.95
0.8	53.94	43.16	2.90
0.8	53.42	42.73	3.85
0.8	52.81	42.24	4.95
0.8	52.28	41.83	5.89
0.8	51.78	41.42	6.90

2.1.2. Mix proportions and mixing procedure

Three series of samples were prepared with water-to-cement (w/c) mass ratios of 0.42, 0.6, and 0.8. Within each series, the AB content ranged from 0 to 7 wt% of the total composite mass. The precise proportions of the mixture for each composition are detailed in Table 1.

The cylindrical sample fabrication process began with the dry mixing of cement and AB powders in a 3D shaker mixer for 30 min to ensure a homogeneous distribution of the filler. The resulting powder was then transferred to an overhead mixer, where deionized water was gradually added to form a homogeneous paste. The fresh paste was cast into cylindrical molds (100 mm height, 20 mm diameter) and subjected to gentle agitation to remove trapped air bubbles. For large tile samples (10 cm ×10 cm ×1 cm), the PNS superplasticizer was added to the mix water prior to its introduction into the powder to ensure adequate workability.

This range was selected to comprehensively capture the material's electrical behavior across the entire percolation transition, from the insulating state below p_c to the well-developed conductive network in the network densification regime. Concentrations above 7 wt% were found to be experimentally impractical, resulting in an unworkable stiff paste due to the extremely high surface area of the AB filler.

It should be noted that the dispersion quality was not quantitatively measured in this study. The chosen dry-mixing method, while standard, may not completely break down all nanoscale agglomerates, as evidenced by some heterogeneity in the final microstructures. While a systematic study of dispersion methods was beyond the scope of this work, it is acknowledged that alternative techniques could yield further improvements [29]. For instance, high-energy methods such as ultrasonication or high-shear mixing of the AB powder in the mix water, particularly in conjunction with optimized superplasticizer dosages, have been shown to be effective in achieving a higher degree of deagglomeration for carbon nanomaterials in cementitious systems. Future work should explore these advanced dispersion strategies to potentially enhance the electrical and mechanical performance of composites.

2.1.3. Curing and final preparation

All samples were demolded after 24 h and cured for 28 days in a sealed chamber at 25 °C and 91% relative humidity, maintained using

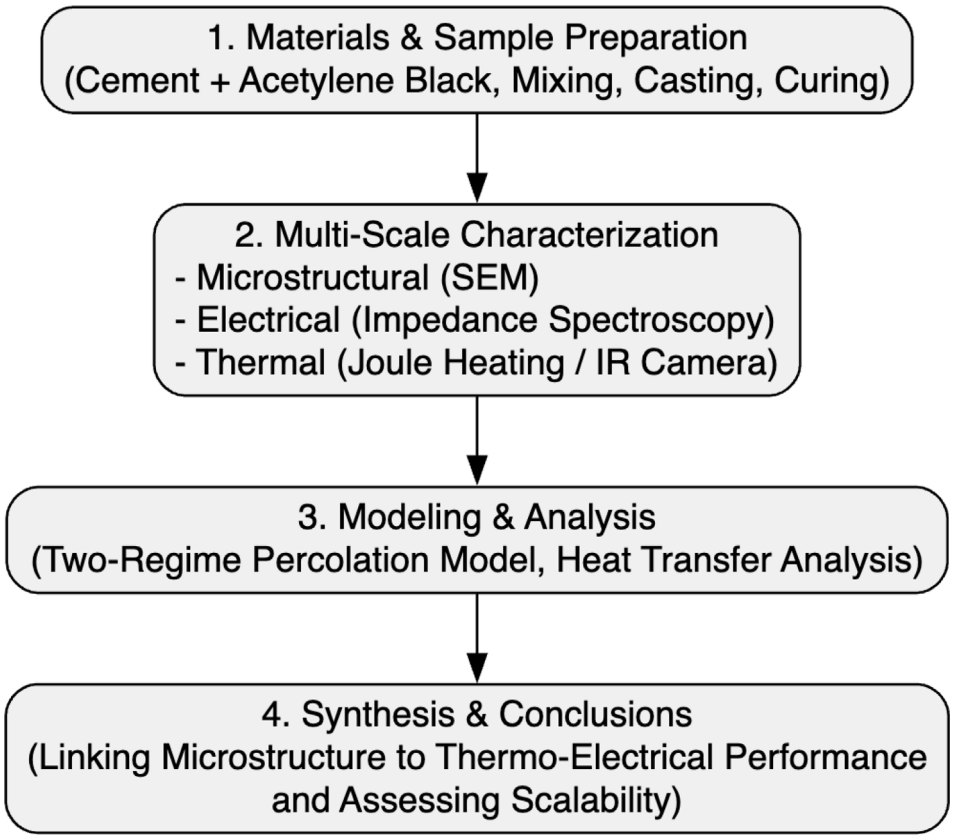

Fig. 1. Flowchart summarizing the experimental and analytical workflow of the study, from material preparation to final thermo-electrical characterization and analysis.

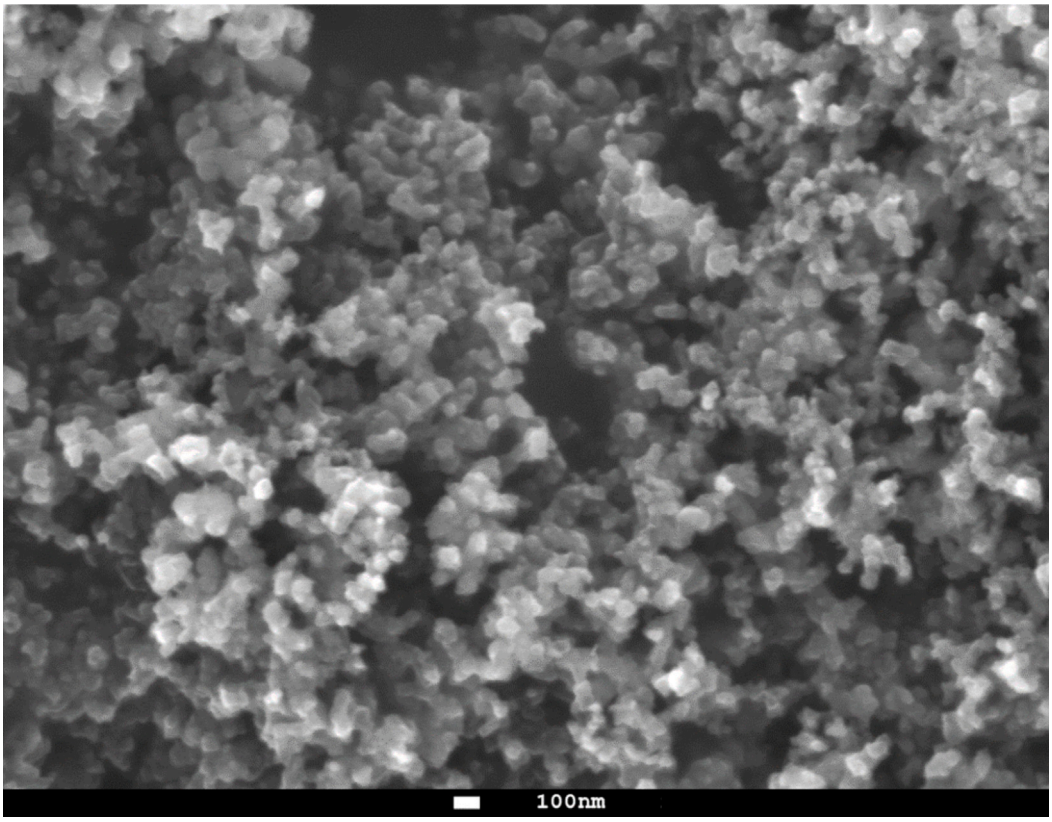

Fig. 2. SEM micrograph of the as-received Acetylene Black powder at 30,000 magnification, showing the morphology of the primary nanoparticles and their aggregation.

a saturated salt solution. Following the curing period, the cylindrical samples were cut into sections with thicknesses of 1 cm and 2 mm for subsequent thermo-electrical characterization. Samples photo is provided in the Supplementary Information (Fig. S3).

These conditions were chosen to provide a stable, standardized environment that promotes full cement hydration while preventing premature drying of the small lab samples. The high relative humidity mimics the sealed internal conditions of larger concrete elements, ensuring the development of a mature and representative cementitious matrix.

2.2. Electrical characterization

The electrical properties of the composites were characterized using electrochemical impedance spectroscopy (EIS). The primary objective of this technique was to determine the bulk electronic resistance of the material, which is dominated by the acetylene black network. To isolate this electronic component from the ionic conductivity contributed by pore water, all samples were first dried in an oven at 60 °C for 24 h prior to measurement.

For measurement, conductive silver paint was applied to the two flat, circular surfaces of each sample (1 cm and 2 mm thick cylinders) to ensure a low-resistance electrical contact. The samples were then placed in a press between two graphite electrodes. The impedance spectrum was acquired using a Solartron Analytical (AMETEK) impedance analyzer. An AC voltage with a root mean square amplitude of 1 V was applied to the sample, sweeping a frequency range from 1 MHz to 0.1 Hz at room temperature to capture the impedance response at different timescales [30]. The use of a small amplitude voltage ensures that the system's response remains within a linear regime [31].

The DC resistance R of each sample was extracted from the resulting Bode plot, an example of which is shown in Fig. 3. In this plot, the impedance magnitude $|Z|$ at very low frequencies plateaus at a constant value. In the same low-frequency region, the phase angle θ approaches 0°, indicating a purely resistive behavior. The DC resistance of the sample R is therefore taken as the value of $|Z|$ on this low-frequency plateau.

From the measured resistance R, the bulk electrical conductivity σ was calculated using the geometry of the sample:

$$\sigma = \frac{L}{R \cdot A} = \frac{L}{R \cdot \pi r^2} \tag{1}$$

where L is the thickness of the sample and A is its cross-sectional area, with radius r.

2.3. Microstructural characterization SEM

The morphology of the received AB powder and the microstructure of the cured AB-cement composites were characterized by Scanning Electron Microscopy. For the composite samples, small fragments were taken from the fractured surfaces of the w/c=0.6 samples containing 2 wt% and 3 wt% AB after 28 days of curing. The micrographs of the sample were acquired with a JEOL JSM-7900F scanning electron microscope at 5 kV. The samples are bonded with double-sided carbon tape and are not covered with a carbon deposit. The presence of carbon in the cement paste ensures good electrical conduction.

2.4. Joule heating characterization

The thermo-electrical response of the composites under an applied voltage (Joule effect) was quantified using infrared thermography (IRT). This non-destructive technique allows for the continuous, full-field monitoring of the sample's surface temperature distribution. A FLIR A6500sc thermal camera, equipped with a Stirling-cooled detector and a 50 mm focal length optical lens, was used for all measurements.

The experimental setup is shown schematically in Fig. 4(a). For each test, a conductive composite sample was placed side-by-side with a non-conductive reference sample (plain cement paste, 0% AB) of the same w/c ratio. The samples were held in a bench press between two expanded graphite electrodes, which provided both electrical contact and mechanical stability. To ensure good electrical contact, the sample surfaces in contact with the electrodes were coated with conductive silver paint. This idealized lab setup, using flat-surface samples with conductive paint and consistent pressure, was intentionally designed to minimize the electrode-sample contact resistance. This ensures that the measured thermo-electrical properties reflect the intrinsic bulk performance of the material, separate from the complex challenges of electrode integration in a practical application. Constant DC voltages of 3 V and 5 V were applied across the test sample using a programmable power supply, while the reference sample was not energized.

Accurate temperature measurement with IRT requires careful calibration and consideration of surface emissivity [32]. To ensure uniform and high emissivity, the top surface of all samples was coated with matte black paint, yielding an emissivity approaching 1. The camera's response was calibrated against a stable and spatially uniform radiation source (a CI Systems SR-80 black body), following established protocols to create a pixel-by-pixel relationship between the detected radiation and the actual temperature [33,34].

During each experiment, a sequence of thermal images was recorded. The raw image data was then processed using custom MATLAB code. For each time step, the average temperature was extracted from a rectangular region of interest (ROI) in the center of both the test sample and the reference sample, as illustrated in Fig. 4(b). Taking a centered rectangle with a width smaller than half the sample diameter insures that the body can be considered as Lambertian with constant emissivity, thus avoiding edge effects and artifacts from the sample boundaries. The net increase in temperature due to Joule heating, $\Delta T(t)$, was then calculated as the difference between the average temperature of the conductive sample and that of the reference sample, which corrects for any minor fluctuations in ambient laboratory temperature.

2.5. Data analysis

Percolation threshold assignment

For each mixture, the percolation threshold p_c was defined in an operational and reproducible manner from the conductivity data. Let p_i denote the carbon black content (in wt.%) and σ_i the corresponding measured conductivity. The baseline point $(p = 0, \sigma = 0)$ was included in all analyses. Instead of assigning p_c by visual inspection of semi-logarithmic plots, we defined p_c as the interpolated concentration at which the conductivity first reaches a reference value of $\sigma = 0.5$ S/m.

More precisely, for each dataset we identified the lowest index i such that $\sigma_i \le 0.5 \text{ S/m} \le \sigma_{i+1}$, and computed

$$p_c = p_i + \left(\frac{0.5 - \sigma_i}{\sigma_{i+1} - \sigma_i} \right) (p_{i+1} - p_i). \tag{2}$$

This definition anchors p_c to the onset of the experimentally observed rise in conductivity, avoids subjective placement of the percolation knee, and can be implemented identically for all water-to-cement ratios and specimen thicknesses. The same procedure was used for both AB composites at 1 cm and 2 mm thickness and for the PBX reference series.

Two-slope power-law model

The conductivity data above the threshold were described by a two-regime power-law model that captures both the rapid increase in conductivity immediately after percolation and the more gradual growth at higher filler contents. For a given dataset, the conductivity $\sigma(p)$ as a function of carbon content p was written as

$$\sigma(p) = \begin{cases} A\,(p - p_c)^{t_1}, & p_c < p \le p^*, \\ A\,(p^* - p_c)^{t_1 - t_2}\,(p - p_c)^{t_2}, & p > p^*, \end{cases} \tag{3}$$

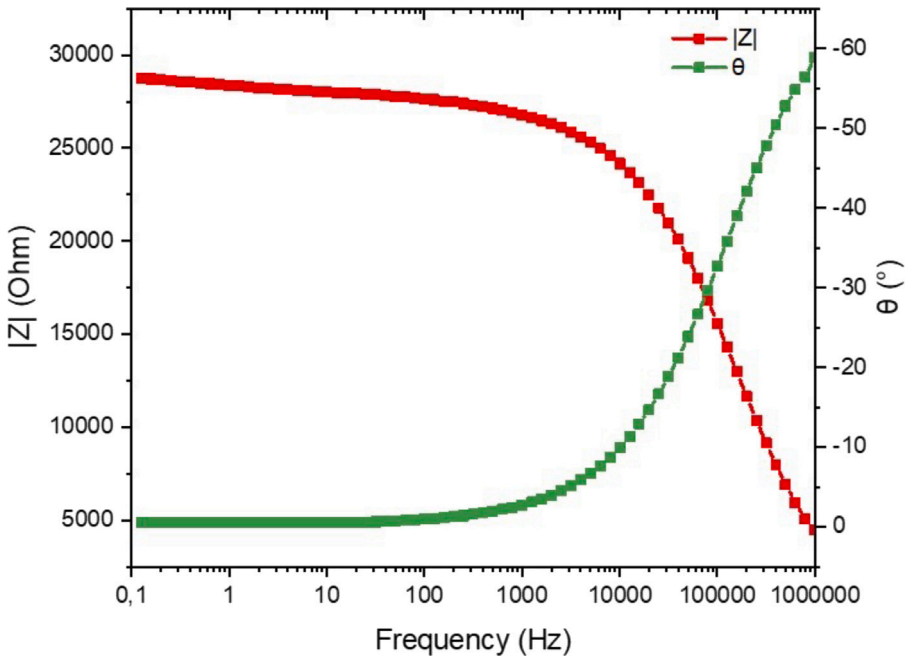

Fig. 3. Example of a Bode plot obtained from an AB-cement composite. The DC resistance R is determined from the impedance magnitude $|Z|$ in the low-frequency region where the phase angle θ approaches zero.

where A is a prefactor, t_1 is the near-threshold transport exponent, t_2 is the post-threshold exponent, and p^* is the crossover concentration separating the two regimes. The continuity factor $(p^* - p_c)^{t_1 - t_2}$ ensures that $\sigma(p)$ is continuous at $p = p^*$. For $p \le p_c$ the conductivity was taken as $\sigma(p) = 0$ in the model.

The parameters $\{t_1, t_2, A, p^*\}$ were obtained by nonlinear least-squares minimization of the weighted sum of squared residuals

$$\chi^2 = \sum_i w_i \left[\sigma_i - \sigma(p_i; A, t_1, t_2, p^*, p_c)\right]^2, \tag{4}$$

where σ_i is the measured conductivity at p_i, $\sigma(p_i;\ldots)$ is the model prediction from Eq. (3), and w_i is a weight reflecting the experimental uncertainty. For AB composites, where repeated measurements were available, w_i was taken as $1/\Delta\sigma_i^2$ with $\Delta\sigma_i$ the experimental standard deviation at p_i. For data points without reported error bars of the PBX series, a constant weight was used, corresponding to unweighted least squares.

To ensure physically meaningful solutions, the optimization was performed under the constraints $t_1 > 0$, $t_2 > 0$, $A > 0$, and $p^* > p_c$. Initial guesses for t_1 and t_2 were chosen of order unity, and p^* was initially set a few weight percent above p_c but below the maximum measured p. The prefactor A was initialized from the order of magnitude of the conductivity in the post-threshold regime. The same fitting procedure and constraint set were applied systematically to each dataset, using the p_c values defined in the previous subsection.

The two-regime representation in Eq. (3) follows the standard crossover form used in percolation theory and composite conductivity models, where the critical near-threshold regime transitions to a higher-loading regime dominated by contact formation and network densification [19,35–37].

Estimation of uncertainties by bootstrap resampling

Uncertainties in the fitted parameters and in the model curves were quantified by bootstrap resampling. For a given dataset $\{p_i, \sigma_i, \Delta\sigma_i\}$ and fixed p_c, we generated an ensemble of synthetic datasets by drawing

$$\sigma_i^{(b)} = \sigma_i + \delta_i^{(b)}, \tag{5}$$

where $\delta_i^{(b)}$ is a random perturbation sampled from a normal distribution of zero mean and standard deviation $\Delta\sigma_i$. For points without reported $\Delta\sigma_i$ (e.g. the PBX series), a small effective noise level was automatically assigned as the larger of $0.05\,\sigma_i$ or 0.02 S/m. This prevents bootstrap samples from becoming artificially noise-free and ensures numerically stable refits. For each bootstrap index $b = 1, \ldots, N_{\mathrm{boot}}$, the two-slope model of Eq. (3) was refitted to $\{\sigma_i^{(b)}\}$ using the same weighted nonlinear least-squares procedure and constraints as for the original data, yielding a collection of parameter sets

$$\left\{t_1^{(b)},\ t_2^{(b)},\ A^{(b)},\ p^{*(b)}\right\}_{b=1}^{N_{\mathrm{boot}}}. \tag{6}$$

From these bootstrap ensembles we computed, for each parameter, the mean value, standard deviation, and empirical confidence intervals (CIs). Unless stated otherwise, the quoted parameter uncertainties correspond to the 16th and 84th percentiles of the bootstrap distributions, which approximate one-standard-deviation CIs for approximately symmetric distributions. For visualization of the model curves, the bootstrap ensemble was also evaluated on a dense grid of p values to obtain the median predicted conductivity and the 2.5th and 97.5th percentiles, which define a 95% confidence band around the best-fit two-slope curve.

Joule heating dynamics

The characteristic time of heat exchanges τ was determined by fitting the temperature evolution data $\Delta T(t)$ from the Joule heating experiments to a first-order exponential rise to a maximum. This model corresponds to the analytic solution of the heat equation in the case of a homogeneous heat source when heat exchanges have been linearized by introducing the τ parameter (see Supplementary Information for the full derivation). An example of this procedure is shown in Fig. 5, where the experimental data (red curve) are fitted to the model (blue curve) described by the following equation:

$$\Delta T(t) = \Delta T_{max}(1 - e^{-t/\tau}) \tag{7}$$

where T_0 is the initial ambient temperature, ΔT_{max} is the maximum steady-state temperature increase, and τ is the characteristic time constant associated with heat exchanges.

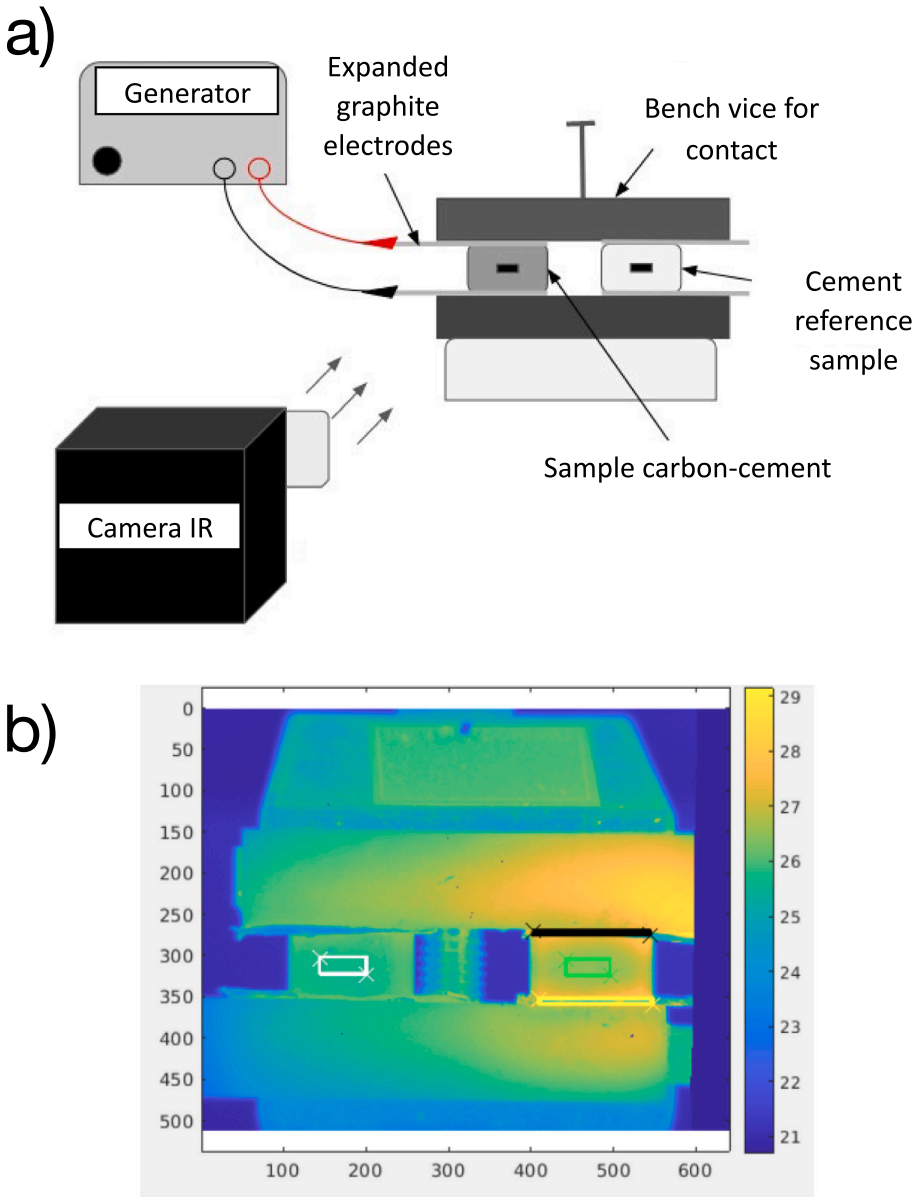

Fig. 4. (a) Schematic of the thermal measurement setup. A non-conductive cement paste sample is used as a reference to correct for ambient temperature changes. (b) Example of a calibrated thermal image showing the regions of interest (white and green rectangular boxes in the center of the samples) from which the average temperature of the conductive sample (right) and reference sample (left) are calculated.

Specific heat capacity calculation

The specific heat capacity c was calculated using the heat balance equation, assuming that all supplied electrical energy was converted to heat within the sample. The formula used was:

$$c = \frac{V^2 \cdot \sigma \cdot \tau}{\Delta T \cdot \rho_c \cdot L^2} \tag{8}$$

where V is the applied voltage, σ is the measured DC electrical conductivity, τ is the characteristic time of heat exchange, and ΔT is the steady-state temperature change obtained by fitting the heating curve with Eq. (7). This equation is derived from the fundamental heat balance, which relates the sample's total heat capacity ($c \cdot \rho_c \cdot V_{\text{sample}}$) to the electrical power input (V^2/R) and the characteristic time of heat exchanges τ (see Supplementary Information for the detailed derivation). The density ρ_c, volume V_{sample} and length between the voltage probes L were determined by direct experimental measurement for each sample.

3. Results and discussion

Complex impedance measurements were used to determine the percolation point and electrical conductivity of all the mixtures studied. The importance of drying samples prior to measurement must be emphasized to decouple electronic conductivity from ionic conductivity, which dominates in moist samples [38–40]. Thermal measurements using IRT were subsequently performed on conductive samples (above the percolation threshold) to evaluate the Joule heating effect.

3.1. Electrical conductivity of cement-carbon composites

The initial phase of this study focused on the influence of carbon filler type and sample size. The choice of carbonaceous filler is known to have a profound impact on the electrical properties of cementitious composites [41]. To quantify this effect, the conductivity of the composites prepared with AB was compared to those made with PBX 135, a common furnace black, at an identical w/c ratio of

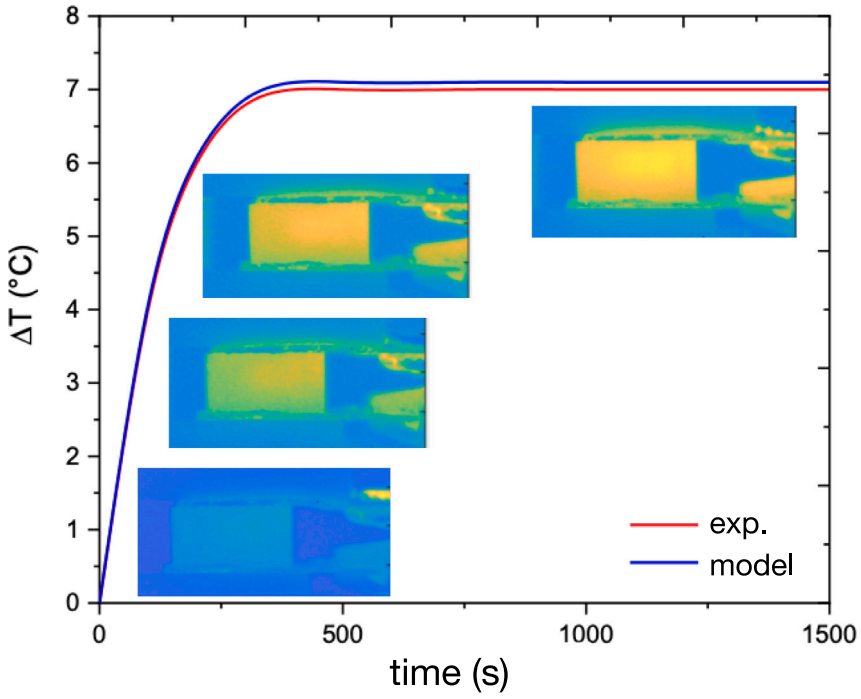

Fig. 5. Example of a temperature evolution curve for a w/c=0.42, 2% wt AB sample under an applied voltage. The experimental data (red) is fitted with the exponential model from Eq. (7) (blue) to extract the steady-state temperature increase ΔT_{max} and the characteristic time τ. Inset images show the corresponding thermal snapshots at different times.

0.42. The results, presented in Fig. 6(a), demonstrate that the AB-based composite achieves significantly higher electrical conductivity at equivalent weight percentages. For example, at 4 wt % loading, the conductivity of the AB composite is nearly triple that of the PBX 135 composite. This highlights the critical role of the filler morphology, a factor that is paramount in all classes of carbonaceous additives, from different grades of carbon black to carbon nanotubes [18].

This better performance is attributed to the distinct multiscale morphology of the AB filler. AB is produced by high-temperature thermal decomposition of acetylene gas, a process that produces a highly pure (> 99% carbon) and highly graphitized nanostructure [21]. At the microscale, these graphitic nanoparticles are fused into high-structure aciniform aggregates (grape-like), which are highly efficient for creating long-range conductive pathways as the grape-like fillers can stack and overlap, increasing the chance of contact. In contrast, furnace blacks such as PBX 135 are produced by partial combustion of heavy oils, typically resulting in a lower degree of graphitization, a more spheroidal aggregate structure, and a higher content of impurities [21, 42]. These spherical fillers require more particles to form enough contacts to reach percolation. The branched and highly graphitic nature of AB facilitates more efficient inter-particle electron transport and allows the formation of a continuous percolation network at a lower volume fraction than the less-structured PBX 135 [43]. Based on its superior efficiency and purity, AB was selected as the conductive filler for all subsequent detailed investigations.

Before analyzing the percolation behavior, it was essential to confirm that the electrical measurements represent a true bulk material property, independent of the sample geometry. To this end, the conductivity of the composites was measured for all three w/c ratios on samples of two different thicknesses: 2 mm and 1 cm. As shown in Fig. 6(b), there is no significant systematic variation in conductivity between the two thicknesses throughout the range of AB concentrations. This result confirms that finite-size or surface effects are negligible in this experimental setup and that the measurements accurately reflect the intrinsic bulk conductivity of the material.

The conductivity trends in Fig. 6(b) exhibit the characteristic non-linear rise expected from a percolation transition, in which a continuous conductive network forms only after the filler content exceeds a critical threshold [19,20]. Applying the operational definition from the Methods section — namely, the interpolated concentration at which the conductivity reaches $\sigma = 0.5$ S/m — we find that PBX exhibits a *higher* percolation threshold than AB. PBX requires approximately 4–5 wt% filler to reach $\sigma = 0.5$ S/m, whereas the AB systems reach this level at significantly lower concentrations (p_c = 1.5–2.8% depending on the water-to-cement ratio). This higher p_c reflects the less efficient connectivity of PBX aggregates, whose lower graphitization, more spheroidal morphology, and weaker interparticle contacts delay the formation of a continuous conductive network within the cement matrix.

Given the markedly superior conductivity and network efficiency of AB, and its clear and reproducible percolation behavior across specimen thicknesses, the subsequent quantitative analysis of the percolation laws focuses exclusively on the AB composites. The AB series provide replicated measurements with error bars and exhibit consistent trends between the 1 cm and 2 mm samples, enabling a robust extraction of percolation thresholds, scaling exponents, and the crossover between conduction regimes in the sections that follow.

Percolation behavior and two-regime conductivity evolution

To quantify the conduction mechanisms activated by the addition of AB, the conductivity data were analyzed using a two-regime percolation model in which the conductivity follows one power law immediately above the percolation threshold and a second power law after the conductive network has consolidated. Fig. 7 presents the conductivity curves for all three w/c ratios (1 cm thickness) together with the bootstrap-averaged two-slope fits and their 95% confidence bands. The fitted parameters for each mixture are summarized in Table 2. These results provide a consistent description of the percolation behavior across the composites.

For all mixtures, conductivity remains negligible up to a critical AB content, after which a sharp increase is observed. The threshold increases systematically with water-to-cement ratio, from approximately

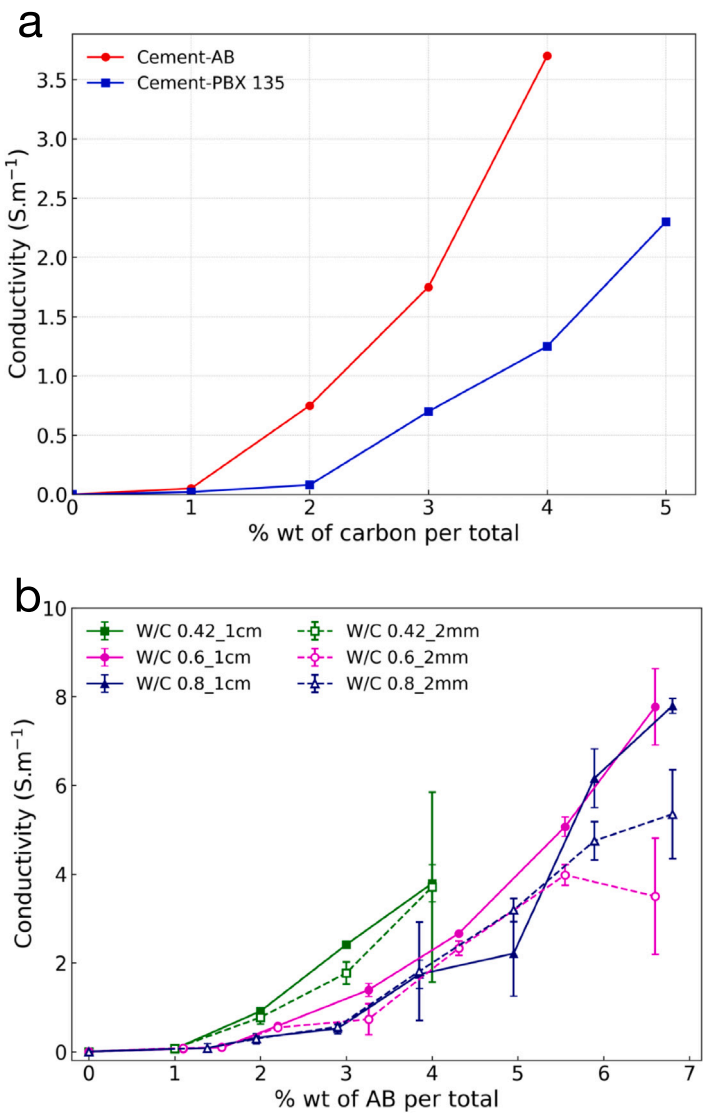

Fig. 6. (a) Comparison of the electrical conductivity of cement composites (w/c = 0.42) prepared with AB versus furnace black PBX 135. The AB-based composite exhibits significantly higher conductivity at equivalent weight percentages, demonstrating its superior efficiency in forming a conductive network. (b) Validation of conductivity measurements on AB-cement composites of two different thicknesses (1 cm and 2 mm) across all three w/c ratios. Error bars represent the standard deviation of measurements on three replicate samples prepared with the same composition.

1.5–1.6 wt% at w/c = 0.42 to around 2.7–2.9 wt% at w/c = 0.80. This trend is expected: mixtures with higher w/c contain more pore space and a more dilute solid skeleton, requiring a larger amount of conductive filler to establish a sample-spanning pathway. The bootstrap confidence bands show that the onset of conductivity is tightly constrained at w/c = 0.42 and 0.80, whereas the w/c = 0.60 series exhibits larger uncertainty at high AB contents due to scatter in a small number of measurements. For this reason, the exponents in that specific dataset are reported but interpreted with caution.

Immediately above the threshold, all mixtures exhibit a rapid activation of conductivity that is captured by the near-threshold exponent t_1. The fitted values $t_1 \approx 0.4$–0.9 indicate a sharp and cooperative onset of charge transport, consistent with the formation of the first sample-spanning backbone of AB aggregates. Beyond a composition-dependent crossover point p^*, the conductivity increases more gradually and follows a second power law with exponent $t_2 \approx 1.3$–1.7. This second regime reflects network densification: as additional AB is added, clusters merge, interparticle gaps shrink, and a greater fraction of the conductive network becomes engaged in low-resistance pathways. This interpretation is supported by the SEM observations discussed later, which also show the transition from a tenuous initial network to a denser and more space-filling conductive phase.

Overall, the combination of Fig. 7 and Table 2 provides a coherent and internally consistent quantitative picture of the conductive behavior of AB–cement composites. The two-regime description captures both the sharp onset of conduction and the subsequent structural consolidation of the network, while the systematic increase of p_c with w/c ratio confirms the role of mixture porosity in governing the formation of a spanning conductive pathway.

The trends observed in Fig. 7 and Table 2 are consistent with percolation-controlled conduction reported in a broad range of composite materials. In ideal lattice models, the conductivity follows a single universal power law near the threshold [19], but real heterogeneous systems frequently display non-universal exponents and multiple regimes because transport is influenced by tunneling distances, contact resistance, aggregate morphology, and matrix heterogeneity. Such non-universal and multi-regime behavior is well documented in carbon-black–polymer composites [22,44,45], where the conductivity often increases sharply at the onset of connectivity and then follows a smoother, curvature-dominated evolution as the network consolidates.

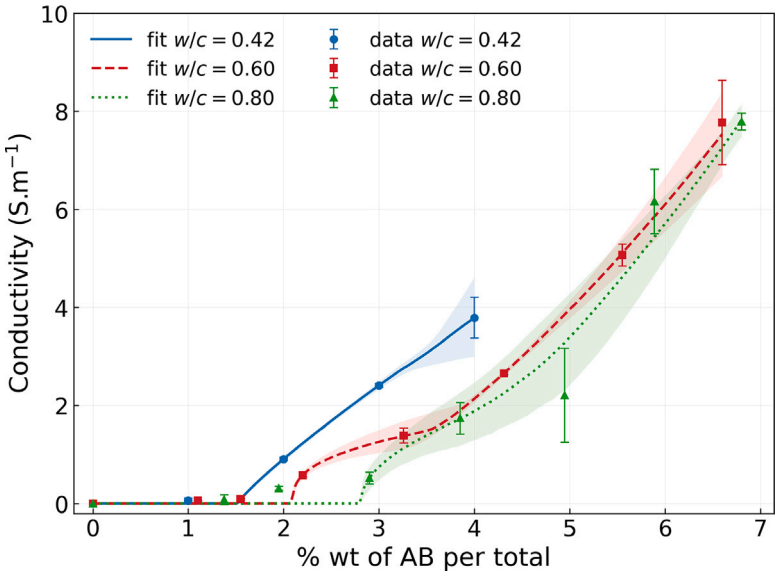

Fig. 7. Electrical conductivity of AB–cement composites (1 cm thickness) as a function of acetylene black content for three water-to-cement ratios. Symbols with error bars denote experimental measurements, while the solid, dashed, and dotted curves represent the median two-slope percolation fits obtained by bootstrap resampling. Shaded regions indicate the 95% confidence bands of the fitted model. The combined plot highlights (i) the increase of the operational percolation threshold p_c with w/c ratio and (ii) the consistent two-regime behavior across mixtures, with a sharp conductivity onset near p_c followed by a smoother, nonlinear densification regime above p^*.

Table 2
Percolation fit parameters for AB composites from two-slope model.

W/C	Thickness	p_c	t_1	t_2	p^*	A	R^2
0.42	1 cm	1.52	0.87	0.92	3.77	1.71	0.9997
0.42	2 mm	1.61	0.65	1.99	3.40	1.43	0.9995
0.60	1 cm	2.09	0.36	1.47	3.62	1.31	0.9988
0.60	2 mm	2.14	0.45	0.29	5.55	1.87	0.8823
0.80	1 cm	2.81	0.49	1.40	4.39	1.71	0.9722
0.80	2 mm	2.69	0.69	0.99	4.20	1.63	0.9890

Typical effective transport exponents in CB- and CNT-filled polymers span $t \simeq 1$–5, and several studies report a clear change of slope in log–log conductivity curves as the conductive phase evolves from a sparse backbone to a denser, more space-filling network [46,47]. This behavior has been linked to two concurrent mechanisms: (i) tunneling-limited charge transfer immediately above p_c, which produces a sharp activation of conductivity, and (ii) progressive contact formation and cluster–cluster coalescence at higher filler contents, which drive a more gradual increase. The values found in the present work align with this picture: the near-threshold exponent t_1 reflects the rapid formation of the first spanning backbone of AB aggregates, while the post-threshold exponent t_2 captures the subsequent structural consolidation of the network.

Comparable observations have been made in cementitious systems. Carbon black, graphite, and CNT–cement composites typically exhibit percolation thresholds of a few weight percent and effective exponents in the range $t \approx 1$–2, reflecting the strong influence of contact resistance, percolation morphology, and the distribution of conductive clusters [8,48,49]. The comparatively low thresholds and moderate exponent values obtained for the AB–cement composites studied here are consistent with the high structure, high graphitization, and aciniform morphology of acetylene black, which favor early connectivity and efficient network densification at modest filler contents.

Together, these comparisons reinforce the interpretation that the two-regime model used in this study captures physically meaningful features of the evolving conductive network. The exponent t_1 quantifies the initial onset of connectivity, while t_2 describes the subsequent thickening and homogenization of the conductive phase as AB loading increases. The systematic variation of p_c with w/c ratio observed in this work is therefore consistent with both the microstructural features of the AB filler and with trends reported in other cement-based conductive composites.

To relate the two-regime percolation behavior to the underlying microstructure, the w/c = 0.6 composites were examined by SEM at key AB loadings (Fig. 8). The micrographs provide visual evidence for both the initial formation of a spanning conductive skeleton and the subsequent consolidation of the AB network as the filler content increases.

Figs. 8(a) and 8(b) show the composite at 2 wt% AB, close to the operational percolation threshold determined from the conductivity analysis. At lower magnification (Fig. 8(a)), the AB appears as a lightly connected, web-like arrangement of fine agglomerates distributed around the larger hydration products. Although sparse, this network spans the porous matrix, consistent with the sharp onset of conductivity captured by the near-threshold exponent t_1.

The higher magnification view (Fig. 8(b)) resolves the nanoscale organization of these agglomerates, where individual AB particles form thin coatings along the surfaces of C–S–H clusters and other hydration phases. In this state, many particle–particle junctions are separated by narrow gaps or thin hydration layers, which likely give rise to the defective, tunneling-dominated contacts responsible for the relatively modest conductivity immediately above p_c.

At 3 wt% AB (Fig. 8(c)), just beyond the crossover concentration p^*, the microstructure changes noticeably. The AB-rich domains become denser, filling a larger fraction of the interstitial space and forming thicker connections between neighboring clusters. This increased packing and improved contact quality correspond to the second conductivity regime characterized by exponent t_2, in which the conductive network no longer consists of tenuous links but instead of robust, multi-path clusters that reduce interfacial resistance.

3.2. Joule heating performance of AB-cement composites

Beyond the fundamental DC conductivity, the integration of conductive fillers into cement opens the door to advanced thermal functionalities. While significant research has explored the thermo-electric

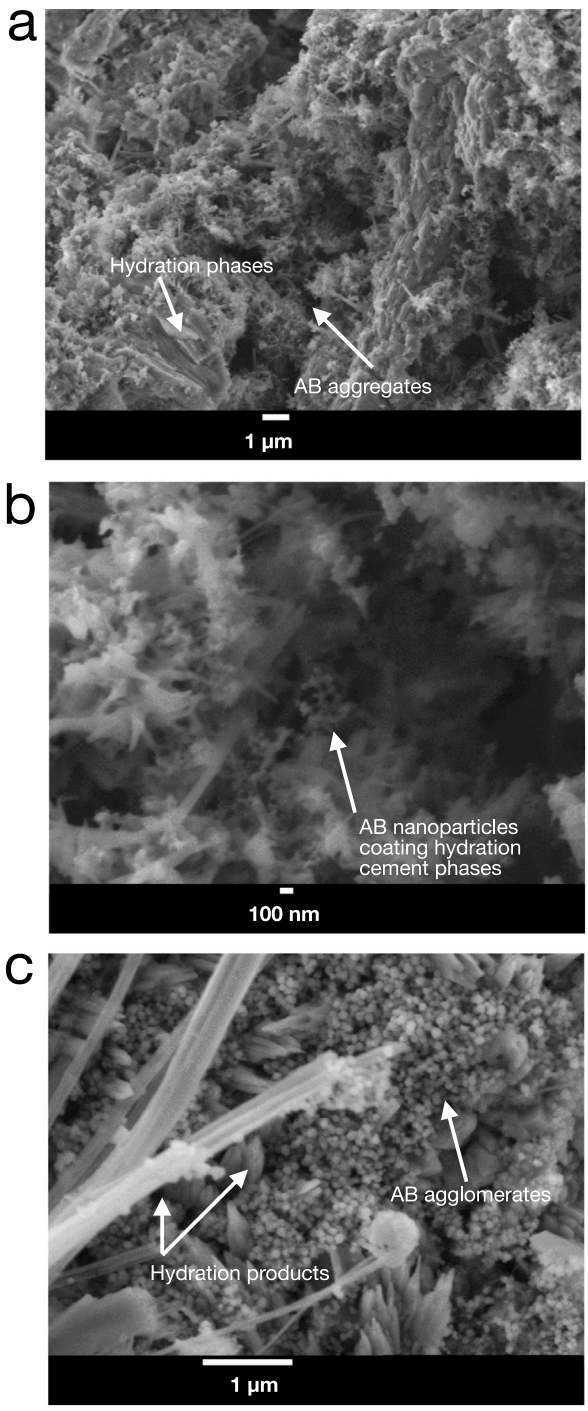

Fig. 8. Representative SEM micrographs of the AB-cement composite (w/c = 0.6) at key AB loadings. (a) At the percolation threshold (2 wt% AB, 6,000×), the composite shows a sparse, web-like arrangement of AB agglomerates forming the first sample-spanning conductive skeleton. (b) At higher magnification (30,000×), individual AB nanoparticles are seen coating hydration phases, creating numerous thin, high-resistance junctions consistent with the near-threshold regime. (c) Just above the crossover concentration (3 wt% AB, 20,000×), the AB-rich domains appear denser and more cohesive, forming thicker contacts and partially filling interstitial spaces. This morphological consolidation corresponds to the second, higher-conductivity regime identified in the percolation analysis. Images are representative of multiple areas measured for each sample.

properties of such composites for energy harvesting and sensing [50, 51], the present work focuses on the material's capacity for Joule heating. This property, governed by the power P dissipated as heat according to the relation $P = V^2/R$, is critical for applications such as self-heating pavements for de-icing or enhanced-curing concrete. For the linearized thermal model introduced previously, the temperature variation in the steady state is proportional to the power dissipated by Joule effect. To characterize the performance of the composites, both the temperature increase ΔT and the characteristic time for heat exchanges τ were investigated using IR thermography.

The primary Joule heating results are summarized in Fig. 9. The steady-state temperature increase as a function of AB concentration is presented in Fig. 9(a). For all w/c ratios, ΔT generally increases with AB content, a direct consequence of the decreasing bulk resistance of the material which allows for a higher current flow at a fixed voltage. However, a clear trend of diminishing returns is evident, with the temperature gain becoming much less pronounced at concentrations above approximately 5 wt%, effectively forming a plateau. It is noted that the $w/c = 0.42$ sample at 4 wt% AB shows a lower ΔT than at 3 wt%. This deviation is attributed to material heterogeneity; dispersing high loadings of nano-fillers like AB homogeneously in a low w/c cement paste is notoriously difficult and can lead to localized agglomerates that disrupt the global conductive network. The use of chemical admixtures, such as polycarboxylate-based superplasticizers, has been shown to significantly improve the dispersion of carbon particles in cementitious systems, which could mitigate such effects at higher concentrations [29].

To better understand the underlying physical mechanisms, the temperature increase ΔT was plotted directly against the measured conductivity σ, as shown in Fig. 9(b). This view reveals two distinct linear regimes, analogous to the two conduction regimes identified in the conductivity analysis. In the initial rapid-onset Ohmic regime, characterized by the low exponent t_1 (at lower conductivity), a small increase in conductivity yields a very large increase in heating. Once the network densifies and transitions to the network densification regime, characterized by the exponent t_2(at higher conductivity), the relationship becomes much shallower; further increases in conductivity produce a more moderate gain in temperature. This observation of two distinct linear regimes in the Joule heating response provides strong, self-consistent evidence for our model. It does not contradict the linearity of the thermal model, but rather reveals a transition between two effective composite materials. The first steep slope corresponds to the near-threshold composite, where heat generation is highly efficient at the resistive junctions. The second, shallower slope represents the network consolidation composite, where the network is more homogeneous. The fact that this thermal behavior aligns perfectly with the two-regime electrical behavior validates that the microstructural evolution of the network governs both properties.

This observed plateau in the maximum temperature gain can be explained by the competing effects of the composite's electrical and thermal properties. As the filler concentration increases into the densification regime, the electrical conductivity and thus the rate of internal heat generation begin to stabilize. Simultaneously, it is well-established that adding conductive carbon fillers also increases the composite's overall thermal conductivity. The rate of heat loss to the environment is proportional to this thermal conductivity. Therefore, a situation arises where the stabilized heat generation is offset by an increasing rate of heat dissipation, causing the steady-state temperature to plateau. This phenomenon is a fundamental thermodynamic equilibrium inherent to multifunctional composites where the filler influences both electrical and thermal transport properties [26].

The dynamics of the heating process and a final validation of the analysis are presented in Fig. 10. The characteristic time of heat exchanges is a critical parameter for practical applications like de-icing pavements, underfloor heating, or thermal energy storage, where rapid response is often desired. It also impacts energy efficiency and thermal

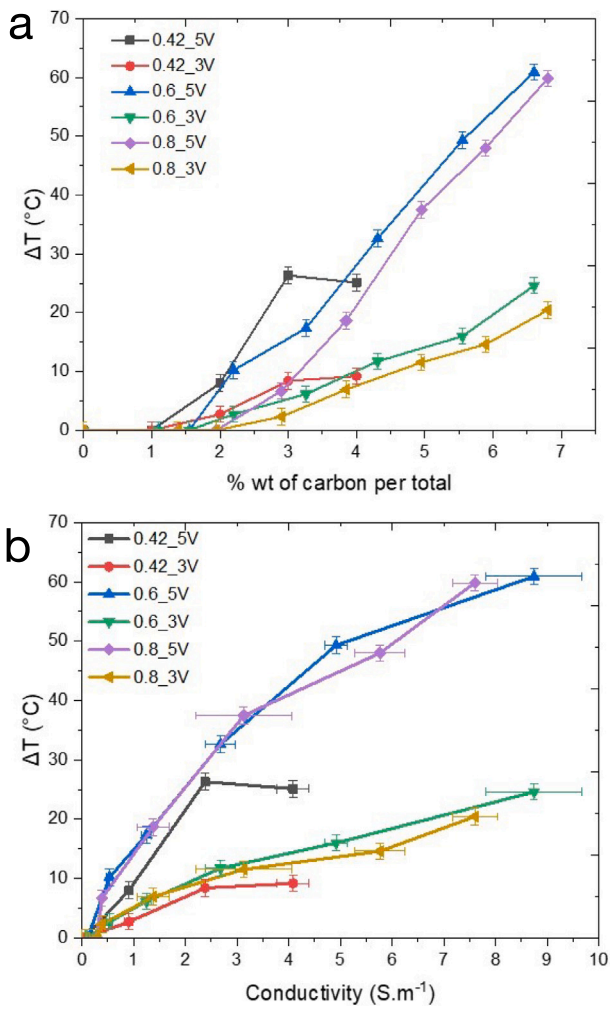

Fig. 9. Joule temperature increase of the AB-cement composites. (a) Steady-state temperature increase ΔT as a function of AB weight percentage for all three w/c ratios under applied voltages of 3 V and 5 V for 1 cm thickness samples. (b) The same ΔT data plotted as a function of the measured bulk conductivity. This representation reveals the underlying relationship between the material's electrical state and its heating performance. Two distinct regimes are observed, analogous to the conduction mechanisms identified previously: an initial steep rise in temperature corresponding to the near-threshold regime, followed by a smaller slope in the network consolidation regime. Error bars represent the standard deviation of measurements on three replicate samples prepared with the same composition.

management, as slower heating implies longer operation times and potential for thermal stress gradients. The characteristic time of heat exchanges τ is plotted as a function of AB content in Fig. 10(a). A clear trend is observed: as the concentration of AB increases, the materials heat up significantly faster (lower τ). This is an expected consequence of the thermo-electrical relationship, where the characteristic time τ is inversely proportional to the electrical conductivity σ, as shown in the heat balance analysis (Eq. (8)). This highlights a critical engineering trade-off: the composite with the highest conductivity provides the fastest heating, but not necessarily the highest final temperature. It is important to note that for a fixed composition, the characteristic time τ is an intrinsic thermal property of the system (dependent on geometry, material properties, and convection) and is independent of the applied electrical power.

To provide a final, robust validation of this entire analysis, the specific heat capacity c of the composites was calculated from the experimental data using the heat balance equation (8). Since the specific heat capacity is an intrinsic material property, it should remain relatively constant across all samples. Fig. 10(b) plots the calculated specific heat as a function of AB content. Despite the large variations in the measured electrical and thermal parameters, the calculated values for c are relatively stable across the range of compositions, falling mostly between $1500\,J\,kg^{-1}\,K^{-1}$ to $3000\,J\,kg^{-1}\,K^{-1}$. This range is notably higher than the typical values reported for standard cement pastes ($840–1170\,J\,kg^{-1}\,K^{-1}$) [52,53]. While the intrinsic specific heat of AB is similar to that of cement, the composite exhibits an apparent enhanced heat storage capacity. This finding, while higher than expected for conventional pastes, is not without precedent in nanoengineered cementitious systems. For instance, a recent study by Dimov et al. on ultrahigh performance graphene-concrete also reported a significant (88%) increase in the material's heat capacity [27]. This suggests that the presence of a well-dispersed carbon nanostructure can fundamentally alter the composite's thermal properties. This apparent enhancement may be attributed to nanoscale phenomena such as enhanced thermal energy storage at the vast carbon-cement interfaces. Alternatively, given that the specific heat of C-S-H is known to be sensitive to its C/S ratio, another plausible cause is a localized shift in the stoichiometry of the C-S-H that preferentially nucleates on the carbon surfaces. While the origin of this enhancement warrants further investigation, the internal consistency of the calculation and its corroboration by other studies provides a robust validation of the entire thermo-electrical measurement and analysis framework.

3.3. Scalability and application perspective

To explore the scalability of these findings for applications like heated flooring, larger tile samples (10 cm ×10 cm ×1 cm) were fabricated using a w/c ratio of 0.42 and 3 wt% AB. A polynaphthalene sulfonate (PNS) based superplasticizer was used to improve the workability and dispersion during mixing, as high AB content significantly increases paste viscosity. Joule heating tests at 5 V showed modest temperature increases (6 °C to 7 °C) and significantly longer characteristic times (1000 s to 1350 s) compared to the small cylindrical samples, primarily due to the larger dimensions and mass, as detailed in Table 3.

While the simple, linearized thermal model is no longer strictly applicable to the complex heat transfer in these larger samples, the same calculation was performed to provide an indicative comparison. As shown in Table 3, despite the different scale, the estimated specific heat capacities remained in the higher range observed previously ($1690\,J\,kg^{-1}\,K^{-1}$ to $1920\,J\,kg^{-1}\,K^{-1}$). This suggests a degree of internal consistency, but these values for τ and c should be considered indicative estimates rather than precise measurements. The spatial distribution of the generated heat was monitored using thermal imaging, as shown in Fig. 11. The time series images confirm that Joule heating is successfully generated, originating at the graphite electrodes and gradually propagating into the bulk of the sample. However, the final thermal image after two hours Fig. 11(c) reveals a non-uniform temperature distribution, with clear hot spots or preferential heating paths forming between the electrodes. While heating is expected in this region, achieving a homogeneous temperature profile across a large surface area is a known challenge in scaled-up resistive heating elements. This observation underscores the importance of optimizing not only the bulk material properties but also the electrode configuration to ensure uniform power dissipation for practical applications. In our scaled-up tile, the electrodes were embedded within the composite, a method that introduces its own challenges in ensuring a consistent, low-resistance interface for good electron flow. A more representative thermal model, including 3D conduction and convection, would be required for a full quantitative description of these complex temperature fields.

To provide a quantitative benchmark against other technologies, we analyzed the intrinsic heating efficiency of our material using the voltage-independent Normalized Power Density metric ($W{\cdot}m^{-2}{\cdot}V^{-2}$),

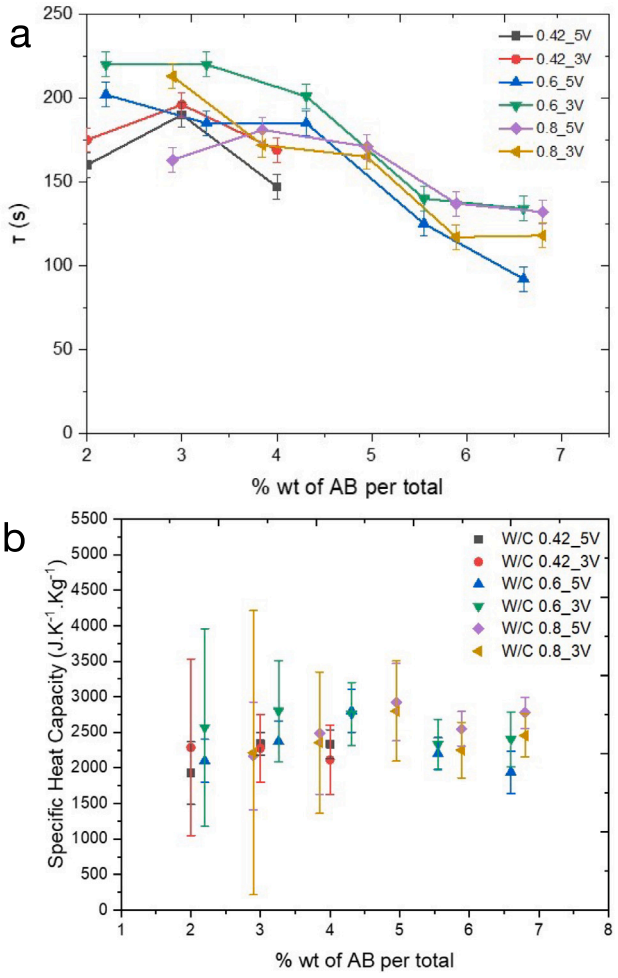

Fig. 10. (a) Characteristic time of heat exchanges τ as a function of AB weight percentage. For all samples, τ decreases with increasing AB content, indicating that more conductive composites heat up more rapidly. Error bars represent the standard deviation of measurements on three replicate samples prepared with the same composition. (b) Specific heat capacity calculated from the experimental data using the linearized heat balance equation at steady state. The values remain relatively constant, independent of filler loading or electrical properties, clustering within a physically plausible range for cementitious composites. Error bars were calculated using standard error propagation from the measurement uncertainties of three replicate samples.

Table 3
Thermo-electric properties of large tile samples (w/c 0.42, 3 wt% AB) with PNS addition for workability.

Property	Tile 1 (0.17% PNS/AB)	Tile 2 (0.28% PNS/AB)
σ (S m^{-1})	1.88	0.90
ΔT at 5V (°C)	6.37	6.92
τ (s)	1010	1353
c (J kg^{-1} K^{-1})	1690	1920

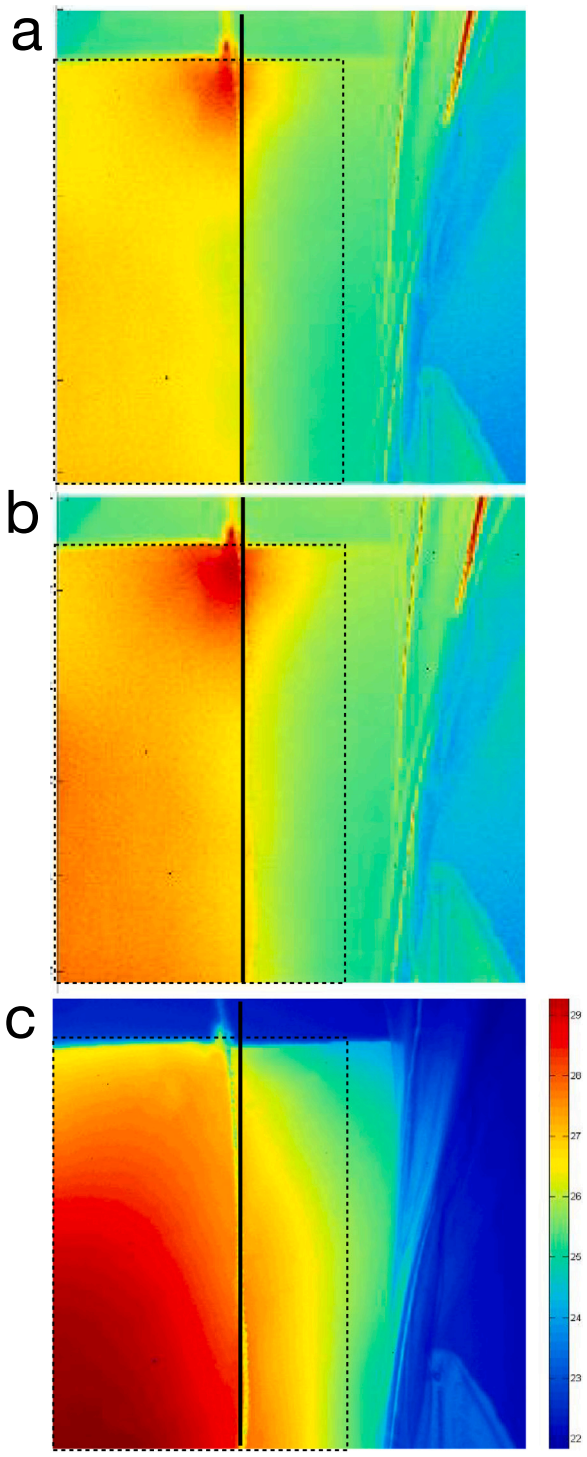

Fig. 11. Thermal imaging of a large tile sample (w/c = 0.42, 3 wt% AB) during Joule heating at an applied voltage of 5 V. The time-series images show the spatial evolution of the temperature profile. (a) At an early stage, heating originates near the top of the graphite electrode. (b) At an intermediate time, the heat begins to propagate into the bulk of the composite. (c) The final thermal image after two hours shows the steady-state temperature distribution. Dashed lines indicate the approximate location of the sample and solid lines the graphite electrodes.

with results summarized in Table 4. Direct comparison between studies is challenging due to variations in geometry, materials, and applied voltage, which significantly impact performance. For instance, applications requiring human contact often use safer, lower voltages (~50 V), while large-scale infrastructure may use higher grid voltages (> 200 V). Despite these complexities, the normalized metric provides a basis for comparing intrinsic material efficiency. The analysis reveals that our lab-scale AB composite possesses an exceptionally high intrinsic efficiency (~850 W·m^{-2}·V^{-2}). More importantly, our unoptimized, scaled-up tile (~1.88 W·m^{-2}·V^{-2}) still demonstrates an intrinsic efficiency that is over 30 times higher than other scaled-up carbon black systems [12] and over 150 times higher than the conductive

Table 4
Comparison of thermo-electrical performance metrics. Power Density is the measured power output per unit of heated surface area (W/m^2). Normalized Power Density is the power density per volt squared ($W \cdot m^{-2} \cdot V^{-2}$), providing a voltage-independent measure of surface heating efficiency.

System	Power Density (W/m^2)	Normalized Power ($W \cdot m^{-2} \cdot V^{-2}$)	Voltage (V)	Reference
This Work (AB, Lab-Scale)	~21,250	~850	5	This Work
This Work (AB, Tile)	~47	~1.88	5	This Work
Carbon Black (Floor Heating)	124	~0.05	50	[12]
Conductive Concrete (Deicing)	500	~0.012	208	[54]
Carbon Fiber (EIH Curing)	667	N/A	N/A	[56]
Embedded CF Wires (Deicing)	300	Not Stated	Not Stated	[46]

concrete used in the Roca Spur Bridge field project [54]. For context, the power density targets for practical applications are demanding, with studies on embedded carbon fiber wires for deicing requiring 300–350 W/m^2 [46,55], and electric-curing applications requiring over 600 W/m^2 [56]. Our analysis confirms that while our lab prototypes have not yet produced this level of total power, their high intrinsic efficiency suggests that they have strong potential to meet these requirements with further engineering, such as applying higher, more practical voltages.

Several strategies could be implemented to address these challenges and provide a clear path forward. For instance, transitioning from the bar electrodes used in this study to alternative geometries, such as an embedded conductive mesh or full-surface plate electrodes, would create a more uniform electric field and mitigate current crowding [7]. Furthermore, while a PNS superplasticizer was used, more advanced dispersion methods such as ultrasonication or high-shear mixing during fabrication could break down nanoparticle agglomerates more effectively, leading to a more homogeneous conductive network [18]. Finally, the development of hybrid filler systems, combining AB with higher aspect-ratio fillers like short carbon fibers, could enhance long-range connectivity, bridging resistive gaps and promoting a more even distribution of current across large surface areas [57]. Future work should focus on systematically evaluating these engineering solutions to translate promising lab-scale results into robust, large-scale applications.

From a practical standpoint, while advanced fillers like CNTs face significant cost and dispersion challenges, AB provides a more viable, cost-effective solution for large-scale applications. Future work could also explore hybrid systems combining AB with carbon fibers to create synergistic improvements in performance [57]. For example, a recent study by Gwon et al. on such hybrid composites demonstrated a synergistic effect, achieving a surface temperature of 77 °C at just 20 V with an optimized mix of carbon black and carbon fibers [58].

In addition to performance considerations, the choice of conductive filler carries practical trade-offs in terms of cost and scalability. While high-aspect-ratio nanomaterials such as carbon nanotubes or graphene nanoplatelets can offer very high intrinsic conductivity, they remain significantly more expensive and present well-documented challenges related to dispersion, often requiring high-energy mixing or chemical functionalization. By contrast, acetylene black is an industrially mature, widely available filler that can be incorporated using standard cement mixing procedures, making it a more viable and cost-effective option for large-volume applications such as pavement heating or de-icing systems. This practical accessibility is an important motivation for the present study and for the potential deployment of AB-based systems at scale.

Furthermore, a comprehensive assessment of long-term durability is a critical next step for validating these materials. The stability of the conductive network under repeated thermal cycling and its performance under freeze-thaw conditions are paramount for de-icing applications. Additionally, long-term chemical changes in the matrix, such as continued hydration and carbonation, are known to alter the pore structure and could disrupt the conductive pathways. Indeed, it has been shown that carbonation can significantly increase the electrical resistivity of cement-nanocarbon composites by precipitating insulating phases within the conductive network [59]. Future work must include systematic durability testing to quantify the robustness of these functional properties, as these combined degradation mechanisms could impact the material's long-term reliability.

4. Conclusion

The key findings and practical insights from this systematic investigation of acetylene black (AB) cement composites are summarized as follows:

- The highly branched, aciniform morphology of acetylene black makes it a significantly more effective conductive filler than standard furnace black, enabling the creation of conductive networks at lower concentrations, which is a key insight for material selection.
- The composite's thermo-electrical behavior is governed by a two-regime percolation model, demonstrating a transition from an exceptionally efficient rapid-onset state (low exponent t_1) to a complex network densification regime (higher exponent t_2). This framework accurately explains the observed performance plateau in heating performance at high filler loadings and provides a critical basis for optimizing filler content to balance performance against material cost.
- A quantitative comparison with literature benchmarks, using a voltage-independent metric, reveals that the AB composite possesses a superior intrinsic heating efficiency compared to other carbon-based systems, highlighting its strong potential for developing highly energy-efficient heating elements.
- While lab-scale performance is excellent, scaled-up applications present significant engineering challenges. Achieving uniform heat distribution requires careful optimization of electrode configurations and filler dispersion, which are key directions for future work to translate these findings into practical technologies.

CRediT authorship contribution statement

Fairouz Touati: Writing – original draft, Visualization, Software, Investigation, Formal analysis, Data curation. **Daniel Ferry:** Writing – review & editing, Visualization, Investigation, Data curation. **Olivier Grauby:** Writing – review & editing, Visualization, Investigation, Data curation. **Philippe Papet:** Writing – review & editing, Validation, Supervision, Resources, Formal analysis, Data curation. **Gwenn Le Saout:** Writing – review & editing, Supervision, Resources, Data curation. **Bertrand Wattrisse:** Writing – review & editing, Validation, Supervision, Software, Resources, Methodology, Investigation, Formal analysis, Data curation. **Katerina Ioannidou:** Writing – review & editing, Writing – original draft, Visualization, Validation, Supervision, Resources, Project administration, Methodology, Funding acquisition, Formal analysis, Conceptualization.

Declaration of competing interest

The authors declare the following financial interests/personal relationships which may be considered as potential competing interests: Fairouz Touati reports financial support was provided by TITAN Cement. Katerina (Aikaterini) Ioannidou has patent #US11897813B2 issued to Massachusetts Institute of Technology (MIT), Cambridge, MA (US) - Centre National de la Recherche Scientifique (CNRS), Paris (FR) - Université de Bordeaux, Bordeaux (FR). If there are other authors, they declare that they have no known competing financial interests or personal relationships that could have appeared to influence the work reported in this paper.

Acknowledgments

F.T. gratefully acknowledges the financial support for this work provided by Titan Cement.The authors are also grateful to Roland Pellenq for valuable discussions. The authors would also like to extend their gratitude to Fokion Tasoulas, Marios Katsiotis, Despoina Papargyriou, and Emmanouil Chatzigeorgiou of Titan Cement for their valuable discussions and for generously providing the materials used in this research.

Appendix A. Supplementary data

Supplementary material related to this article can be found online at https://doi.org/10.1016/j.conbuildmat.2025.144822.

Data availability

Data will be made available on request.

References

[1] International Energy Agency (IEA) for the Global Alliance for Buildings and Construction (GlobalABC), Global Alliance for Buildings and Construction 2018 Global Status Report, Tech. rep., UN Environment Programme, 2018, http://www.ren21.net/wp-content/uploads/2018/06/17-8652{_}GSR2018{_}FullReport{_}web{_}final{_}.pdf.

[2] D. Williams, N.E. Williams, Y. Cao, Road salt contamination of groundwater in a major metropolitan area and development of a biological index to monitor its impact, Water Research 34 (1) (2000) 127–138, http://dx.doi.org/10.1016/S0043-1354(99)00129-3, http://www.sciencedirect.com/science/article/pii/S0043135499001293.

[3] E.-L. Thunqvist, Regional increase of mean chloride concentration in water due to the application of deicing salt, Sci. Total Environ. 325 (1) (2004) 29–37, http://dx.doi.org/10.1016/j.scitotenv.2003.11.020, http://www.sciencedirect.com/science/article/pii/S0048969703006740.

[4] M. Kayama, A. Quoreshi, S. Kitaoka, Y. Kitahashi, Y. Sakamoto, Y. Maruyama, M. Kitao, T. Koike, Effects of deicing salt on the vitality and health of two spruce species, picea abies karst.,and picea glehnii masters planted along roadsides in northern japan, Environ. Pollut. 124 (1) (2003) 127–137.

[5] T.R. Menzies, National cost of damage to infrastructure from highway deicing, in: Corrosion Forms and Control for Infrastructure, ASTM International, West Conshohocken, PA, 1992, https://compass.astm.org/DIGITAL_LIBRARY/STP/PAGES/STP19753S.htm.

[6] K. Wang, D.E. Nelsen, W.A. Nixon, Damaging effects of deicing chemicals on concrete materials, Cem. Concr. Compos. 28 (2) (2006) 173–188, http://dx.doi.org/10.1016/j.cemconcomp.2005.07.006, http://www.sciencedirect.com/science/article/pii/S0958946505001010.

[7] A. Oumer, C. Lee, E. Ahn, S. Gwon, Review on self-heating electrically conductive cementitious composites: Focus on deicing and electrical curing, Constr. Build. Mater. 439 (2024) 137232, http://dx.doi.org/10.1016/j.conbuildmat.2024.137232.

[8] F. Sanchez, K. Sobolev, Nanotechnology in concrete–a review, Constr. Build. Mater. 24 (11) (2010) 2060–2071, http://dx.doi.org/10.1016/j.conbuildmat.2010.03.014.

[9] G. Bastos, F. Patiño-Barbeito, F. Patiño-Cambeiro, J. Armesto, Nano-inclusions applied in cement-matrix composites: a review, Mater. (Basel, Switzerland) 9 (12) (2016) 1015, http://dx.doi.org/10.3390/ma9121015, https://pubmed.ncbi.nlm.nih.gov/28774135.

[10] M.E. Maglogianni, P.A. Danoglidis, M.S. Konsta-Gdoutos, Electrical-to-thermal energy conversion efficiency of conductive concrete, Cem. Concr. Compos. 139 (2023) 104992, http://dx.doi.org/10.1016/j.cemconcomp.2023.104992.

[11] C. Chang, M. Ho, G. Song, Y.-L. Mo, H. Li, A feasibility study of self-heating concrete utilizing carbon nanofiber heating elements, Smart Mater. Struct. 18 (12) (2009) 127001, http://dx.doi.org/10.1088/0964-1726/18/12/127001, URL https://iopscience.iop.org/article/10.1088/0964-1726/18/12/127001.

[12] S. Mingqing, M. Xinying, W. Xiaoying, H. Zuofu, L. Zhuoqiu, Experimental studies on the indoor electrical floor heating system with carbon black mortar slabs, Energy Build. 40 (6) (2008) 1094–1100, http://dx.doi.org/10.1016/j.enbuild.2007.10.009, http://www.sciencedirect.com/science/article/pii/S0378778807002356.

[13] J. Gomis, O. Galao, V. Gomis, E. Zornoza, P. Garcés, Self-heating and deicing conductive cement. Experimental study and modeling, Construct. Building Materials 75 (2015) 442–449, http://dx.doi.org/10.1016/j.conbuildmat.2014.11.042, http://www.sciencedirect.com/science/article/pii/S0950061814012616.

[14] P. Tumidajski, P. Xie, M. Arnott, J. Beaudoin, Overlay current in a conductive concrete snow melting system, Cem. Concr. Res. 33 (11) (2003) 1807–1809, http://dx.doi.org/10.1016/S0008-8846(03)00198-4, http://www.sciencedirect.com/science/article/pii/S0008884603001984.

[15] H.F.W. Taylor, Cement chemistry, Thomas Telford, 1997.

[16] H.M. Jennings, Refinements to colloid model of c-s-h in cement: Cm-ii, Cem. Concr. Res. 38 (3) (2008) 275–289.

[17] K. Ioannidou, K.J. Krakowiak, M. Bauchy, C.G. Hoover, E. Masoero, S. Yip, F.-J. Ulm, P. Levitz, R.J.-M. Pellenq, E. Del Gado, Mesoscale texture of cement hydrates, Proc. Natl. Acad. Sci. 113 (8) (2016) 2029–2034, http://dx.doi.org/10.1073/pnas.1520487113.

[18] M.S. Konsta-Gdoutos, Z.S. Metaxa, S.P. Shah, Highly dispersed carbon nanotube reinforced cement based materials, Cem. Concr. Res. 40 (7) (2010) 1052–1059, http://dx.doi.org/10.1016/j.cemconres.2010.02.015.

[19] D. Stauffer, A. Aharony, Introduction To Percolation Theory, Taylor & Francis, 1994.

[20] G.S. Bocharov, A.V. Eletskii, Percolation conduction of carbon nanocomposites, Int. J. Mol. Sci. 21 (20) (2020) 1–25, http://dx.doi.org/10.3390/ijms21207634.

[21] S. Khodabakhshi, P.F. Fulvio, E. Andreoli, Carbon black reborn: structure and chemistry for renewable energy harnessing, Carbon 162 (2020) 604–649, http://dx.doi.org/10.1016/j.carbon.2020.02.058, https://www.sciencedirect.com/science/article/pii/S0008622320302049.

[22] I. Balberg, Tunneling and nonuniversal conductivity in composite materials, Phys. Rev. Lett. 59 (1987) 1305–1308, http://dx.doi.org/10.1103/PhysRevLett.59.1305, https://link.aps.org/doi/10.1103/PhysRevLett.59.1305.

[23] Y. Zare, K.Y. Rhee, Simulation of percolation threshold, tunneling distance, and conductivity for carbon nanotube (cnt)-reinforced nanocomposites assuming effective cnt concentration, Polymers 12 (1) (2020) http://dx.doi.org/10.3390/polym12010114.

[24] P. Sheng, Fluctuation-induced tunneling conduction in disordered materials, Phys. Rev. B 21 (6) (1980) 2180–2195.

[25] M. Farrokhzad, J.-h. Ha, H.-S. Lee, Effects of multidimensional carbon-based nanomaterials on the low-carbon and high-performance cementitious composites: A critical review, Materials 17 (10) (2024) 2196.

[26] J. Liu, Y. Zhang, Y. Leng, Y. Wang, L. Wang, Multifunctional cementitious composites from fabrication to their application in pavement: A comprehensive review, Appl. Sci. 15 (7) (2024) 3451.

[27] D. Dimov, I. Amit, O. Gorrie, M.D. Barnes, N.J. Townsend, A.I.S. Neves, F. Withers, S. Russo, M.F. Craciun, Ultrahigh performance nanoengineered graphene–concrete composites for multifunctional applications, Adv. Funct. Mater. 28 (23) (2018) 1705183, http://dx.doi.org/10.1002/adfm.201705183.

[28] R.J.M. Pellenq, A. Ioannidou, N. Chanut, T. Divoux, R. Backov, F.-J. Ulm, Electron conducting carbon-based cement, 2020.

[29] N. Soliman, K. Ioannidou, T. Divoux, R. Backov, M. Omran, T. Nîrca, R.J.-M. Pellenq, Nano-carbon black (ncb)-dispersed cement composites: A macro-to-nano investigation revealing trade-offs between electrical conductivity and mechanical strength, Constr. Build. Mater. 489 (2025) 142246, http://dx.doi.org/10.1016/j.conbuildmat.2025.142246.

[30] S. Ali, S. Chang, M. Imran, Q. Shi, Y. Chen, H. Zhong, Impedance spectroscopy: a versatile technique to understand solution-processed optoelectronic devices, Phys. Status Solidi (RRL)–Rapid Res. Lett. 13 (5) (2019) 1800580.

[31] E. Barsoukov, J.R. Macdonald, Impedance spectroscopy theory, experiment, and, Applications, second ed., John Wiley & Sons, Inc., Hoboken, NJ, 2005.

[32] A. Chrysochoos, V. Huon, F. Jourdan, J.-M. Muracciole, R. Peyroux, B. Wattrisse, Use of full-field digital image correlation and infrared thermography measurements for the thermomechanical analysis of material behaviour, Strain 46 (1) (2010) 117–130.

[33] B. Berthel, A. Chrysochoos, B. Wattrisse, A. Galtier, Infrared image processing for the calorimetric analysis of fatigue phenomena, Exp. Mech. 48 (2008) 79–90.

[34] V. Honorat, S. Moreau, J.-M. Muracciole, B. Wattrisse, A. Chrysochoos, Calorimetric analysis of polymer behaviour using a pixel calibration of an irfpa camera, Quant. InfraRed Thermogr. J. 2 (2) (2005) 153–171.

[35] S. Kirkpatrick, Percolation and conduction, Rev. Modern Phys. 45 (1973) 574–588, http://dx.doi.org/10.1103/RevModPhys.45.574, https://link.aps.org/doi/10.1103/RevModPhys.45.574.

[36] J.P. Straley, Critical exponents for the conductivity of random resistor lattices, Phys. Rev. B 15 (1977) 5733–5737, http://dx.doi.org/10.1103/PhysRevB.15.5733, https://link.aps.org/doi/10.1103/PhysRevB.15.5733.
[37] A. Celzard, J. Marêché, F. Payot, G. Furdin, Electrical conductivity of carbonaceous powders, Carbon 40 (15) (2002) 2801–2815, http://dx.doi.org/10.1016/S0008-6223(02)00196-3.
[38] M. Liebscher, L. Tzounis, D. Junger, T.T. Dinh, V. Mechtcherine, Electrical joule heating of cementitious nanocomposites filled with multi-walled carbon nanotubes: Role of filler concentration, water content, and cement age, Smart Mater. Struct. 29 (12) (2020) http://dx.doi.org/10.1088/1361-665X/abc23b.
[39] M. Sun, Z. Li, Q. Mao, D. Shen, Study on the hole conduction phenomenon in carbon fiber-reinforced concrete, Cem. Concr. Res. 28 (4) (1998) 549–554, http://dx.doi.org/10.1016/S0008-8846(98)00003-2.
[40] S. Wen, D.D.L. Chung, The role of electronic and ionic conduction in the electrical conductivity of carbon fiber reinforced cement, Carbon 44 (11) (2006) 2130–2138, http://dx.doi.org/10.1016/j.carbon.2006.03.013.
[41] C.-W. Nan, Physics of inhomogeneous conductors, Prog. Mater. Sci. 37 (1) (1993) 1–116.
[42] J.-B. Donnet, Carbon Black: Science and Technology, CRC Press, 1993.
[43] D. Pantea, H. Darmstadt, S. Kaliaguine, C. Roy, Electrical conductivity of conductive carbon blacks: Influence of surface chemistry and topology, Appl. Surf. Sci. 217 (1–4) (2003) 181–193, http://dx.doi.org/10.1016/S0169-4332(03)00550-6.
[44] I. Balberg, D. Azulay, D. Toker, O. Millo, Percolation and tunneling in composite materials, Internat. J. Modern Phys. B 18 (15) (2004) 2091–2121, http://dx.doi.org/10.1142/S0217979204025336.
[45] S. Vionnet-Menot, C. Grimaldi, T. Maeder, S. Strässler, P. Ryser, Tunneling-percolation origin of nonuniversality: Theory and experiments, Phys. Rev. B 71 (2005) 064201, http://dx.doi.org/10.1103/PhysRevB.71.064201, https://link.aps.org/doi/10.1103/PhysRevB.71.064201.
[46] Y. Liu, Y. Lai, D.X. Ma, Melting snow on airport cement concrete pavement with carbon fibre heating wires, Mater. Res. Innov. 19 (sup10) (2015) S10–95–S10–99, http://dx.doi.org/10.1179/1432891715Z.0000000002097.
[47] W. Bauhofer, J.Z. Kovacs, A review and analysis of electrical percolation in carbon nanotube polymer composites, Compos. Sci. Technol. 69 (10) (2009) 1486–1498.
[48] N.A. Soliman, N. Chanut, V. Deman, Z. Lallas, F.-J. Ulm, Electric energy dissipation and electric tortuosity in electron conductive cement-based materials, Phys. Rev. Mater. 4 (2020) 125401, http://dx.doi.org/10.1103/PhysRevMaterials.4.125401, https://link.aps.org/doi/10.1103/PhysRevMaterials.4.125401.
[49] N. Chuewangkam, P. Iadrat, T. Yurata, C. Changtong, S. Pinitsoontorn, Enhancing electrical performance of cement-based materials with acetylene carbon black for paste, mortar and concrete applications, Sci. Rep. 15 (1) (2025) 33552.
[50] L. Tzounis, M. Liebscher, R. Fuge, A. Leonhardt, V. Mechtcherine, P- and n-type thermoelectric cement composites with cvd grown p- and n-doped carbon nanotubes: Demonstration of a structural thermoelectric generator, Energy Build. 191 (2019) 151–163, http://dx.doi.org/10.1016/j.enbuild.2019.03.027.
[51] J. Wei, Q. Zhang, L. Zhao, L. Hao, Z. Nie, Effect of moisture on the thermoelectric properties in expanded graphite/carbon fiber cement composites, Ceram. Int. 43 (14) (2017) 10763–10769, http://dx.doi.org/10.1016/j.ceramint.2017.05.088.
[52] J.-M. Torrenti, J.-M. Reynouard, G. Pijaudier-Cabot, Mechanical Behavior of Concrete, Wiley Online Library, 2010.
[53] V. Waller, Modelling of the Temperature Rise of a Concrete During Its Setting under Adiabatic Conditions, As a Function of Its Formulation (Ph.D. thesis), University of Paris, 1993.
[54] C.Y. Tuan, S.A. Yehia, Implementation of conductive concrete overlay for bridge deck deicing at roca, nebraska, in: Transportation Research Circular E-C063: Snow Removal and Ice Control Technology, 2004, pp. 363–378.
[55] Y. Lai, Y. Liu, D. Ma, Automatically melting snow on airport cement concrete pavement with carbon fiber grille, Cold Reg. Sci. & Technol. 103 (2014) 57–62, http://dx.doi.org/10.1016/j.coldregions.2014.03.008.
[56] J. Xie, Y. Zhang, W. Tian, Z. Zhang, W. Wang, Effect of curing parameter on the performance of electric-induced heating-cured carbon fiber-reinforced conductive cement-based materials: Experiment and finite element method analysis, Materials 18 (2025) 4057, http://dx.doi.org/10.3390/ma18174057.
[57] D. Chung, Electrical conduction behavior of cement-matrix composites, J. Mater. Eng. Perform. 11 (2002) 194–204.
[58] S. Gwon, H. Kim, M. Shin, Self-heating characteristics of electrically conductive cement composites with carbon black and carbon fiber, Cem. Concr. Compos. 137 (2023) http://dx.doi.org/10.1016/j.cemconcomp.2023.104942.
[59] K. Gawel, S. Wenner, L. Edvardsen, Effect of carbonation on bulk resistivity of cement/carbon nanofiber composites, Constr. Build. Mater. 305 (2021) 124794.